Probing neutron–proton effective mass splitting using nuclear stopping and isospin mix in heavy-ion collisions in GeV energy region

Fan Zhang[1] · Jun Su[2]

Abstract The ramifications of the effective mass splitting on the nuclear stopping and isospin tracer during heavy-ion collisions within the gigaelectron volt energy region are studied using an isospin-dependent quantum molecular dynamics model. Three isotope probes, i.e., a proton, deuteron, and triton, are used to calculate the nuclear stopping. Compared to the $m_\mathrm{n}^* > m_\mathrm{p}^*$ case, the $m_\mathrm{n}^* < m_\mathrm{p}^*$ parameter results in a stronger stopping for protons but a weaker stopping for tritons. The calculations of the isospin tracer show that the $m_\mathrm{n}^* > m_\mathrm{p}^*$ parameter results in a higher isospin mix than the $m_\mathrm{n}^* < m_\mathrm{p}^*$ parameter. The rapidity and impact parameter dependences of the isospin tracer are also studied. A constraining of the effective mass splitting using the free nucleons with high rapidity and in a central rather than peripheral collision is suggested.

Keywords Neutron–proton effective mass splitting · Nuclear stopping · Isospin mix

✉ Fan Zhang
zhangfan@mail.bnu.edu.cn

1 Department of Electronic Information and Physics, Changzhi University, Changzhi 046011, China

2 Sino-French Institute of Nuclear Engineering and Technology, Sun Yat-sen University, Zhuhai 519082, China

1 Introduction

Despite wide investigations in both nuclear physics and nuclear astrophysics, the nuclear potential between nucleons is not fully understood [1–4]. There are three degrees of freedom for the nuclear potential, namely the density ρ, momentum $\mathbf{p}$, and isospin asymmetry $\delta = (\rho_\mathrm{n} - \rho_\mathrm{p})/(\rho_\mathrm{n} + \rho_\mathrm{p})$. For the density and isospin dependence, many theoretical and experimental studies have been conducted during the past decades [5–7]. Readers are encouraged to refer to previous reviews on the accepted acknowledge regarding two degrees of freedom [8, 9].

The momentum dependence of the nuclear potential has been recently emphasized [10–12]. For example, it was found that the momentum degree of freedom is requisite in extracting the compressibility of nuclear matter [18]. The momentum dependence of the nuclear potential between a proton and nucleus has been measured and parameterized within an energy range of 10 MeV $<E_\mathrm{kin}<$ 1 GeV [13–17]. Apart from studying the momentum-dependent nuclear potential, the gradient of momentum, i.e., $\mathrm{d}U/\mathrm{d}p$, has also been studied. This is the concept of the effective mass m^* [19]. An isoscalar effective mass of $m^*/m = 0.7 \pm 0.05$ at normal density and the Fermi momentum have been wildly used in transport models [20]. However, the concept of effective mass splitting is applied to describe the difference in the effective masses between a neutron and proton in asymmetric nuclear matter [21–24]. Knowledge regarding neutron–proton (np) effective mass splitting is essential for understanding neutron stars and exotic nuclei [25, 26]. Unfortunately, np effective mass splitting is not fully understood [27–30]. Some theories

have predicted $m_n^* > m_p^*$ in neutron-rich matter [31–33], whereas other theories have made an opposite prediction [34–36].

Effective mass splitting plays an important role in the transport simulation of heavy-ion collisions [37]. There are two main parts in a transport simulation, i.e., the evolution in the mean field and nucleon–nucleon (NN) scattering. The effective mass splitting results in different mean fields of the proton and neutron. Thus, in an energy region of approximately 100 MeV/nucleon, the calculations of the isospin observable in heavy-ion collisions will depend on the effective mass splitting applied in the model. Using the double n/p spectral ratios and isospin diffusion, the role of the effective mass splitting on the mean field has been investigated [37–39]. However, few studies have reported the influence of the effective mass splitting on NN scattering, which is dominant in heavy-ion collisions at an energy level of gigaelectron volts [40–42]. It has been indicated that the effective mass provides an in-medium correction of the NN cross sections [43, 44]. The in-medium factors related to the nucleon effective mass have been widely used in transport models [45–47]. Owing to the effective mass splitting, a splitting of the in-medium factors will occur between the neutron–neutron (nn) and proton–proton (pp) cross sections [48]. Thus, an observable isospin that is sensitive to the NN scattering may depend on the effective mass splitting. The effects of the in-medium NN cross sections on the observable stopping and the ratio of free protons have been found in ^{96}Zr(^{96}Ru) + ^{96}Ru(^{96}Zr) collisions at 400 MeV/nucleon [49]. In this study, an attempt was made to determine the effect of the effective mass splitting on the nuclear stopping and isospin mix in heavy-ion collisions at incident energies of 150 to 1500 MeV/nucleon.

The remainder of this paper is organized as follows. In Sect. 2, the proposed method is described. In Sect. 3, the results are presented and discussed. In Sect. 4, some concluding remarks are given.

2 Theoretical framework

In this study, a similar theoretical framework as that applied in a previous study is used [50]. Readers can refer to the references for the isospin-dependent quantum molecular dynamics (IQMD) model. For brevity, the nuclear potential energy and in-medium corrections to the NN cross sections are discussed here.

The nuclear potential energy is given by the following:

$$U = \int \left[\frac{\alpha}{2} \frac{\rho^2}{\rho_0} + \frac{\beta}{\gamma+1} \frac{\rho^{\gamma+1}}{\rho_0^\gamma} + \frac{g_{sur}}{2} \frac{(\nabla\rho)^2}{\rho_0} \right] d\mathbf{r}$$
$$+ \int \frac{C_{s,p}}{2} \left(\frac{\rho}{\rho_0}\right)^{\gamma_i} \rho \delta^2 d\mathbf{r}$$
$$+ \frac{1}{2\rho_0} \sum_\tau C(1+x) \iiint d\mathbf{p} d\mathbf{p}' d\mathbf{r} f_\tau(\mathbf{r}, \mathbf{p})$$
$$\times \ln^2[\epsilon(\mathbf{p}-\mathbf{p}')^2 + 1] f_\tau(\mathbf{r}, \mathbf{p}')$$
$$+ \frac{1}{2\rho_0} \sum_\tau C(1-x) \iiint d\mathbf{p} d\mathbf{p}' d\mathbf{r} f_\tau(\mathbf{r}, \mathbf{p})$$
$$\times \ln^2[\epsilon(\mathbf{p}-\mathbf{p}')^2 + 1] f_{-\tau}(\mathbf{r}, \mathbf{p}'). \tag{1}$$

Here, ρ is the nucleon density, $\delta = (\rho_n - \rho_p)/(\rho_n + \rho_p)$ is the asymmetry denoted by the neutron density ρ_n and proton density ρ_p, and $f_\tau(\mathbf{r}, \mathbf{p})$ is the phase-space density, with $\tau = -1/2$ for a proton and $\tau = 1/2$ for a neutron. The summation includes both a neutron and proton. The parameters $\alpha = -130$ MeV, $\beta = 59$ MeV, $\gamma = 2.09$, $g_{sur} = 130$ MeV, $C = 1.57$ MeV, and $\epsilon = 0.0005$ c^2/MeV^2 provide a hard equation of state ($K = 380$ MeV) for symmetric nuclear matter [51]. In fact, the commonly accepted value of the compressibility is approximately $K = 240$ MeV. In [17], it has been shown that the calculation of the nuclear stopping using a tiff compressibility of $K = 380$ MeV with a momentum-dependent interaction agrees more with the data than that for a soft case ($K = 200$ MeV) with a momentum dependent interaction. The effective mass splitting rather than the compressibility is focused on, and thus, a compressibility of $K = 380$ MeV is still used.

The effective mass splitting depends on parameter x. The value $x = -0.65$ is applied to provide $m_n^* > m_p^*$ in neutron-rich nuclear matter, and $x = 0.65$ for $m_n^* < m_p^*$. The parameters $C_{s,p} = 23.5$ MeV and $\gamma_i = 1.0$ are used for $x = 0.65$, whereas $C_{s,p} = 52.5$ MeV and $\gamma_i = 1.0$ for $x = -0.65$ to give the same density dependence of the symmetry energy. These parameters have been applied to calculate the nuclear collective flows in the HICs [35, 36]. Refer to Fig. 1 in [35] for the symmetry energy as a function of density, and Fig. 1 in [36] for the lane potential as a function of momentum provided by the parameters. Particularly in asymmetric nuclear matter with $\delta = 0.2$ at the saturation density, $m_n^* > m_p^*$ results in an effective mass of $m_n^*/m = 0.72$ and $m_p^*/m = 0.68$, whereas $m_n^* < m_p^*$ results in effective masses of $m_n^*/m = 0.68$ and $m_p^*/m = 0.72$.

It is worth noting that the integrals of momenta in Eq. (1) are solved by a summation in the code. Meanwhile, the phase-space densities f_τ are reduced to the nucleon
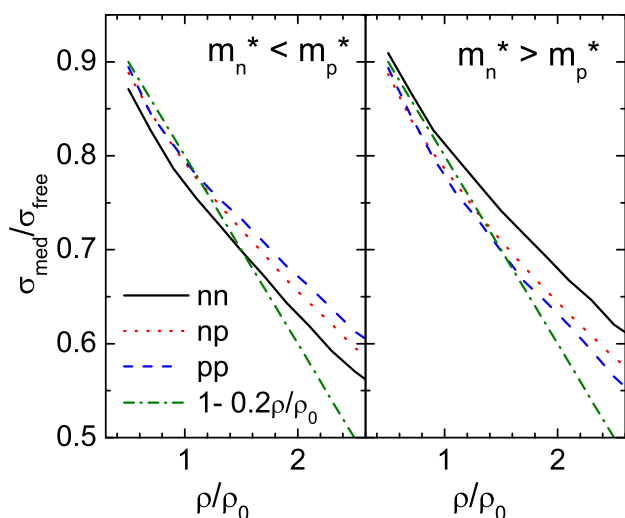
Fig. 1 In-medium factors as a function of density for two colliding nucleons with collision energy $E_{lab} = 400$ MeV at an instant of 20 fm/c in the central reaction of ^{96}Zr + ^{96}Zr with a beam energy of 400 MeV/nucleon

densities, which only depend on the coordinate r. In this case, the difference in the algorithms between the momentum dependence and two body interactions is only the intensities of the interaction between two nucleons. The former intensity depends on the momenta of two nucleons, whereas the latter intensity is $\frac{\alpha}{2\rho_0}$.

In-medium corrections to NN scattering cross sections are needed in the calculations. An isospin independent parametrization, expressed as $f_{NN}^{med} = 1 - 0.2\frac{\rho}{\rho_0}$, has been used in [52]. In this study, the effective mass of each nucleon is calculated from the momentum-dependent potential. Next, the in-medium factor of an NN cross section for ith and jth nucleons is calculated [43–46]

$$f_{ij}^{med} = \frac{\sigma_{med}}{\sigma_{free}} = \left[\frac{m_i^* m_j^* / (m_i^* + m_j^*)}{m_i m_j / (m_i + m_j)} \right]^2, \qquad (2)$$
$$m_i^* = \left[\frac{1}{m_i} + \frac{\partial U}{p_i \partial p_i} \right]^{-1}.$$

The in-medium factor f_{ij}^{med} is an isospin and is energy dependent [see Eq. (1)].

Nucleon colliding pairs with $E_{lab} = 400$ MeV are selected from all simulated events at $t = 20$ fm/c and then applied to calculate the in-medium correction factors to show the isospin dependence. The results for the central reaction of ^{96}Zr + ^{96}Zr at 400 MeV/nucleon are shown in Fig. 1. Two panels correspond to the effective mass splitting of $m_n^* < m_p^*$ and $m_n^* > m_p^*$. The dash-dotted curve is the isospin independent parametrization $1 - 0.2\frac{\rho}{\rho_0}$. The other three curves are the in-medium factors of nn, np, and pp cross sections extracted from the effective masses. The

values of both cases are shown to be similar at subnormal and normal densities. However, in the density region above $1.5\rho_0$, the in-medium factors extracted from the effective masses are globally larger than in the parameterized case.

It can be seen that the free-space cross sections of the nn and pp scattering are the same. However, the in-medium nn cross sections are smaller than those for the pp scattering when using the parameters providing $m_n^* < m_p^*$. Oppositely, $m_n^* > m_p^*$ leads to larger in-medium nn cross sections than the pp case.

Finally, it should be noted that the Pauli blocking algorithm is different compared to that in [50]. The phase-space density f_i' is calculated after the scattering. It is then interpreted as a blocking probability. The probability of $(1 - f_1')(1 - f_2')$ is applied to allow the scattering.

3 Results and discussions

It was determined that nuclear stopping can be influenced by the in-medium effect of NN scattering [49]. The in-medium factor of NN scattering has been calculated from the effective mass splitting in this study [see Eq. (2)]. Thus, the calculation of nuclear stopping is expected to be affected by the effective mass splitting. The stopping of observable *varxz* calculated from the proton, deuteron, and triton rapidity is applied. The definition of the observable *varxz* and the data are referenced from [40],

$$varxz = \frac{\langle y_x^2 \rangle}{\langle y_z^2 \rangle} \qquad (3)$$

where y_x and y_z are the transverse and longitudinal rapidity, respectively. The averages are obtained for the proton, deuteron, and triton. Compared to global nuclear stopping, the stopping observable for the isotopes can provide further insight into the isospin property. As an example, Fig. 2 shows the excitation function of the stopping of observable varxz for the proton, deuteron, and triton produced in central Au + Au collisions ($b < 2$ fm).

The values of *varxz* for three isotopes show a similar rise and fall with the maximum at near 400 MeV/nucleon, which has also been found for the global stopping [41]. The maximum nuclear stopping, which is related to the competition between the mean field, Pauli blocking, and inelastic collisions, is not perfectly reproduced by the model. The phenomenological method for the Pauli blocking may be responsible for this. However, the isotope dependence of the observable *varxz*, which is guided by the dotted line, is reproduced well by the model.

For the same incident energy, more stopping occurs for a proton, less occurs for a triton, and the average amount
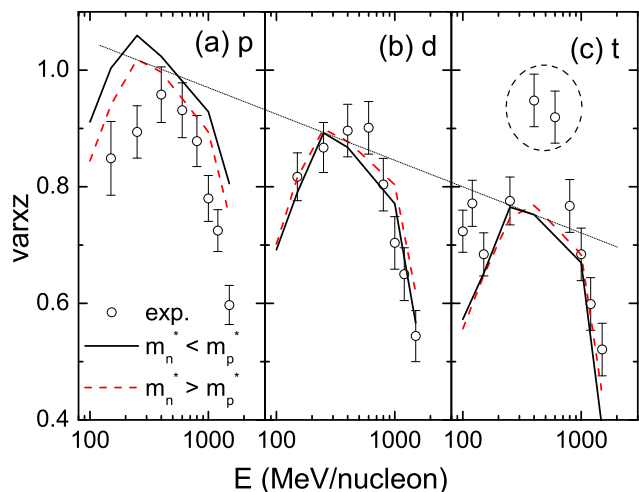
Fig. 2 Excitation function of the stopping observable varxz for the proton, deuteron, and triton produced in central Au + Au collisions ($b < 2$ fm). The data and error taken from [40] are shown as open circles. The solid and dashed curves show the calculations in the cases of $m_n^* < m_p^*$ and $m_n^* > m_p^*$, respectively. The dotted line indicates the guiding of the isotope dependence of the observable varxz. The dashed circle indicates two data points that deviate from the system

occurs for a deuteron. It should be noted that there are two data points deviating from the systematic nature of isotope dependence (shown in the dashed circle). The model does not reproduce such abnormal increases.

In Fig. 3, the stopping of observable varxz is shown as a function of the system mass. The systems ^{40}Ca + ^{40}Ca, ^{58}Ni + ^{58}Ni, ^{96}Ru + ^{96}Ru, ^{129}Xe + ^{131}I, and ^{197}Au + ^{197}Au, and incident energies of 150 to 1500 MeV/

nucleon, are considered. For the FOPI data, the central events are sorted based on the ratio of total kinetic energy between the transverse and longitudinal directions. As indicated by the FOPI collaboration, the dependence of the system size on the nuclear stopping is observable for studying the transparency of the nuclei. The data support the transparency of the nuclei and incident energies involved. All three isotope probes show that lighter nuclei have higher transparency. Moreover, the dependence of the system size is more obvious in a higher incident energy region (see Fig. 24 in [40]). Two aspects may be responsible for the system size dependence of nuclear stopping. First, a peripheral collision has more transparency than a central collision. The central collision is defined by $b < 0.15\, b_{max}$, where the maximum $b_{max} = 1.15(A_p^{1/3} + A_t^{1/3})$ fm is approximate. The system mass and incident energy dependencies of b_{max} may influence the centralities of the sorted events. Second, the surfaces of the nuclei are more transparent than the core with normal density. For light nuclei, the proportion of the surface is larger than the core case. Note the fact that the mean field, i.e., the long-range effect, dominates the nuclear stopping at a low incident energy. The long-range effect allows the core to stop more of the surface. This may be responsible for the weak system size dependence of the nuclear stopping at low energy.

Regarding the effect of the effective mass splitting, note the global difference between the solid and dashed curves in Fig. 2. Owing to more pp scatterings provided by the $m_n^* < m_p^*$ case than the $m_n^* > m_p^*$ case (referring to Fig. 1),
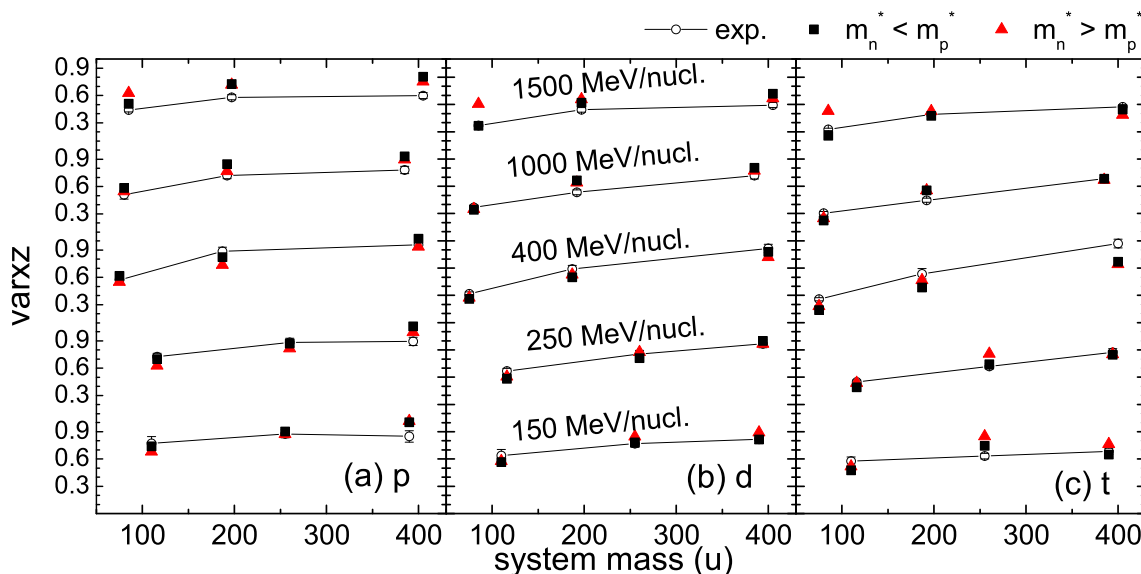

Fig. 3 Stopping of observable varxz for proton, deuteron, and triton produced in central HICs ($b < 0.1725(A_p^{1/3} + A_t^{1/3})$), shown as a function of the system mass. The open circles with error bars show the

data taken from [40]. The squares and triangles show the calculations in the cases of $m_n^* < m_p^*$ and $m_n^* > m_p^*$, respectively

the $m_n^* < m_p^*$ results in a stronger stopping for the proton, as shown in Fig. 2a. Through a similar inference to nn scatterings, a stronger stopping for neutron and neutron-rich fragments is expected when $m_n^* > m_p^*$ is considered in the calculation. Similar effects can be observed for all reaction systems in Fig. 3. For the proton probe, as shown in Fig. 3a, the squares representing the $m_n^* < m_p^*$ case are globally at the top of the triangles representing the $m_n^* < m_p^*$ case. The effect globally for the triton probe can be seen in Fig. 3c. However, the effect is too weak compared to the error bars in the data.

To show this effect more clearly, the observable differences in the proton and triton are shown in Fig. 4. Once again, the squares representing the $m_n^* < m_p^*$ case are globally at the top of the triangles representing the $m_n^* < m_p^*$ case. However, it cannot be concluded which case reproduces the data better because the errors in the data are too large compared to the effect of the effective mass splitting.

Another observation related to the amount of rapidity is proposed in [42]. The relative abundance of the free protons was adopted to trace the isospin mixing between the projectile and target nucleons

$$R_Z = \frac{2Z^{\text{mix}} - Z^{\text{Zr}} - Z^{\text{Ru}}}{Z^{\text{Zr}} - Z^{\text{Ru}}}, \tag{4}$$

where Z^{mix}, Z^{Zr}, and Z^{Ru} are the number of free protons in reactions of $^{96}\text{Ru} + ^{96}\text{Zr}$ (or $^{96}\text{Zr} + ^{96}\text{Ru}$), $^{96}\text{Zr} + ^{96}\text{Zr}$, and $^{96}\text{Ru} + ^{96}\text{Ru}$, respectively. In the case of full equilibrium in the mixed reactions $^{96}\text{Ru} + ^{96}\text{Zr}$ and $^{96}\text{Zr} + ^{96}\text{Ru}$, the value of R_Z is zero.
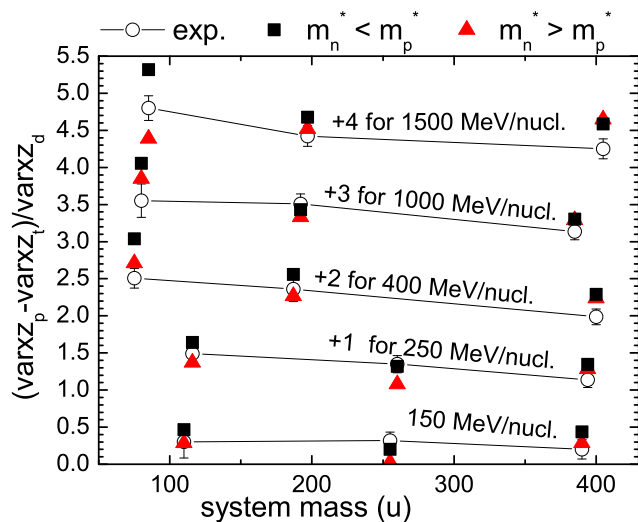

Fig. 4 Difference in observable varxz probing using a proton and triton, normalized by that for a deuteron. The symbols for incident energies of 250, 400, 1,000, and 1500 MeV/nucleon are translated by values of 1, 2, 3, and 4, respectively
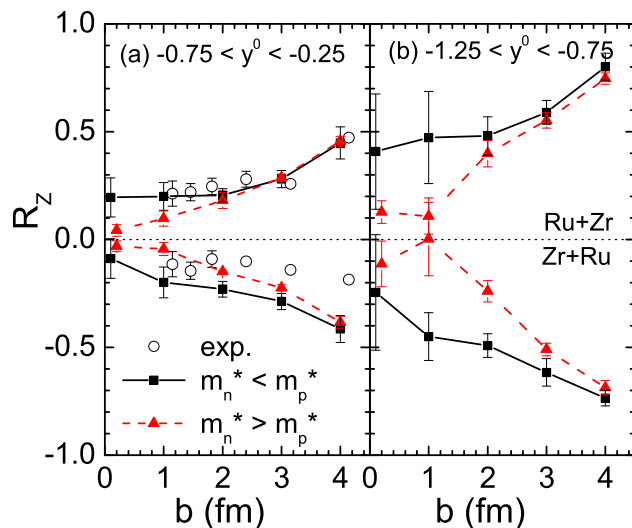

Fig. 5 Centrality dependence of R_Z within the rapidity ranges **a** $-0.75 < y^0 < -0.25$ and **b** $-1.25 < y^0 < -0.75$ for both $^{96}\text{Ru} + ^{96}\text{Zr}$ and $^{96}\text{Zr} + ^{96}\text{Ru}$ reactions, respectively, at 400 MeV/ nucleon. The circles show the data taken from [42]

The centrality dependence of R_Z for both $^{96}\text{Ru} + ^{96}\text{Zr}$ and $^{96}\text{Zr} + ^{96}\text{Ru}$ reactions at 400 MeV/nucleon has been determined using FOPI collaboration, for which a rapidity range of $-0.75 < y^0 < -0.25$ is considered [42]. The proton and $t/^3\text{He}$ are applied as the probes, as shown in Figs. 5 and 6. It can be seen that the nonzero R_Z for $^{96}\text{Ru} + ^{96}\text{Zr}$ and $^{96}\text{Zr} + ^{96}\text{Ru}$ appear to be symmetric relative to the axis $R_Z = 0$, supporting an image of incomplete isospin equilibration. Moreover, the difference between two mixed reactions increases slightly with the impact parameter. Compared to those in the peripheral collisions, the temperatures and densities are higher in a
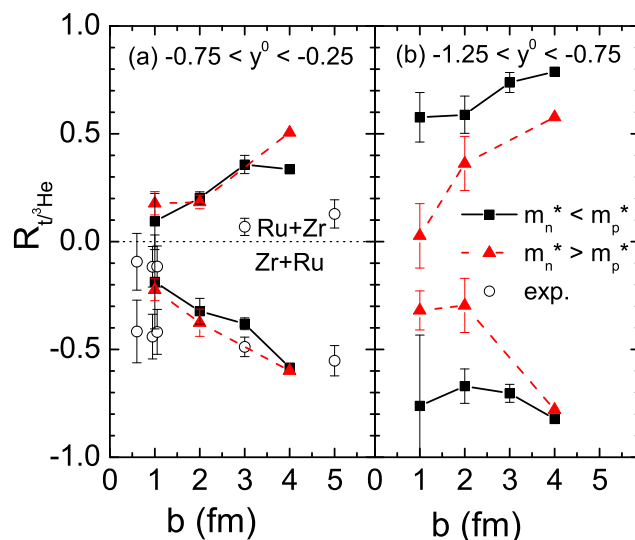

Fig. 6 Similar to Fig. 5 but for a $t/^3\text{He}$ probe

central collision. Hence, there is less mixing in the peripheral collisions and more mixing in the central collisions.

Using the IQMD model, the values of R_Z are calculated using the free protons in the rapidity ranges of $-0.75 < y^0 < -0.25$ (shown in Fig. 5a) and $-1.25 < y^0 < -0.75$ (shown in Fig. 5b), respectively. The center of each square or triangle is the average of those five simulated groups, whereas the error bar refers to the standard deviation. In Figs. 5a and 6a, the effect of the effective mass splitting can be seen. However, the effective mass splitting cannot be constrained because the calculations for $m_n^* > m_p^*$ and $m_n^* < m_p^*$ are similar and generally agree with the data. Interestingly, most values for $m_n^* > m_p^*$ are closer to zero than the $m_n^* < m_p^*$ case, except for $b = 4.0$ fm. The divergences in R_Z between the two calculations are more obvious for a larger rapidity ($-1.25 < y^0 < -0.75$) and at a smaller centrality. This indicates that the observable R_Z for fast protons in the central collisions is sensitive to the effective mass splitting.

The rapidity dependence of R_Z for central $^{96}Ru + {}^{96}Zr$ reactions at 400 MeV/nucleon was determined using FOPI collaboration [42], as shown in the circles in Fig. 7. The data for negative rapidity are available. Because of the reaction symmetry, the data are shown for $^{96}Zr + {}^{96}Ru$ in a positive rapidity region. The data show approximately zero values of R_Z at midrapidity ($y^0 \approx 0$), with positive values on the $y^0 < 0$ side and negative values on the $y^0 > 0$ side. The positive values of R_Z indicate that the protons in this rapidity cell are predominantly populated from the Zr
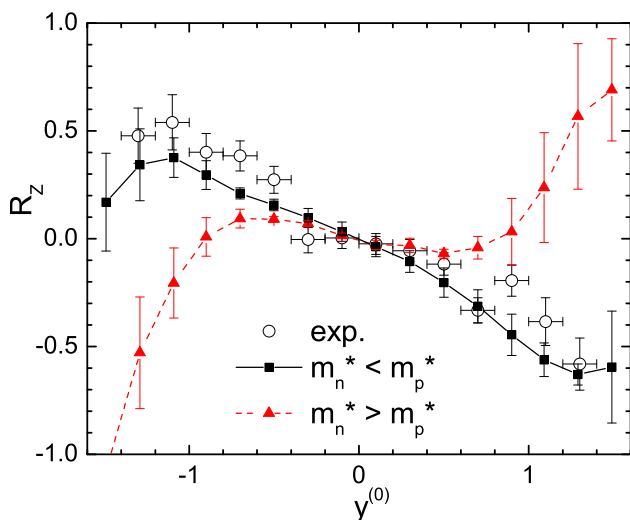
target, whereas the negative values indicate they are populated from a Ru projectile [42].

To investigate the sensitivity of R_Z to the effective mass splitting, simulations with $m_n^* < m_p^*$ and $m_n^* > m_p^*$ are conducted, respectively. Here, the number of events of each group is 300,000. In fact, the symmetry energy is also expected to affect the isospin mixings, but there is no difference between when a soft or stiff symmetry energy is applied to the calculation. In fact, during the compression phase, with the nucleon density approaching approximately $2\rho_0$, soft parameters provide a stronger repulsion of protons than stiff parameters because the colliding system is neutron-rich. However, in a stiff central collision at 400 MeV/nucleon, the NN scatterings are violent. The similar values of R_Z for soft and stiff symmetry energies support the hypothesis that the effect of the local symmetry potential to an isospin tracer is reduced by the violent NN scatterings.

The calculations for $m_n^* < m_p^*$ and $m_n^* > m_p^*$ are shown as squares and triangles in Fig. 7, respectively. It can be seen that the results for $m_n^* > m_p^*$ show more isospin stoppings, and even an over balance, whereas $m_n^* < m_p^*$ is more appropriate for reproducing the data. Our results in Fig. 1, together with the calculations in [45, 46], have shown that $m_n^* > m_p^*$ results in a larger in-medium factor under more scattering than $m_n^* < m_p^*$. This could be the dynamic reason for more proton mixing for $m_n^* > m_p^*$ than for $m_n^* < m_p^*$ because violent NN scattering, rather than the mean field, is responsible for the isospin mixing. Figure 7 shows the robust effect of the effective mass splitting on the isospin tracer for the central collision and high rapidity region. However, other effects on the isospin tracer, such as those of the compressibility and Pauli blocking, should be investigated before using the isospin tracer data to constrain the effective mass splitting.

4 Conclusion

In summary, the effects of the effective mass splitting on the nuclear stopping during heavy-ion collisions within a gigaelectron volt energy region were studied within the IQMD model. Three isotope probes, i.e., proton, deuteron, and triton, were used to calculate the nuclear stopping. Compared to the $m_n^* > m_p^*$ case, the $m_n^* < m_p^*$ parameter results in a stronger stopping for a proton but a weaker stopping for triton. The opposite influences of the effective mass splitting on the proton–proton and neutron–neutron scatterings may be responsible for the above phenomenon. However, it is worth mentioning that, not only the number, but also the angular distribution of the scattering influences

Fig. 7 Isospin tracer R_Z as a function of rapidity for a central $^{96}Ru + {}^{96}Zr$ reaction at 400 MeV/nucleon. The data are taken from [42]. The solid and dashed curves show the calculations in the cases of $m_n^* < m_p^*$ and $m_n^* > m_p^*$, respectively

the nuclear stopping. The effect of the effective mass splitting on the angular distribution was further studied.

The effect of the effective mass splitting on the isospin tracer was also considered. The calculations of the isospin tracer show that the $m_n^* > m_p^*$ parameter results in more isospin mixing than the case of $m_n^* < m_p^*$. In fact, the effects of the effective mass splitting on the nuclear stopping and isospin tracer were investigated in [49], using the central $^{96}Ru + ^{96}Zr$ collision at 400 MeV/nucleon. Compared to [49], the innovations in this study are as follows. The effect of the effective mass splitting on the nuclear stopping is ubiquitous in $^{40}Ca + ^{40}Ca$, $^{58}Ni + ^{58}Ni$, $^{96}Ru + ^{96}Ru$, $^{129}Xe + ^{131}I$, and $^{197}Au + ^{197}Au$ at incident energies of 150, 250, 400, 1,000, and 1,500 MeV/nucleon. The system mass dependence shows that the effect is stronger in a lighter system. However, the effect is quite weak compared to the error in the data, although the differences in the varxz values between a proton and triton are used to intensify the effect. Concerning the isospin mixing, the impact parameter and the dependence on the rapidity were studied using a proton and the ratio between ^3H and ^3He as the probes. It was found that the effect of the effective mass splitting on an isospin tracer is the strongest for a central collision and in a high rapidity region. However, other effects on the isospin tracer, such as those of the compressibility and Pauli blocking, should be investigated before using the isospin tracer data to constrain the effective mass splitting.

References

1. H.A. Bethe, Supernova mechanisms. Rev. Mod. Phys. **62**, 801 (1990). https://doi.org/10.1103/RevModPhys.62.801
2. A.W. Steiner, M. Prakash, J.M. Lattimer et al., Isospin asymmetry in nuclei and neutron stars. Phys. Rep. **411**, 325 (2005). https://doi.org/10.1016/j.physrep.2005.02.004
3. P. Danielewicz, R. Lacey, W.G. Lynch, Determination of the equation of state of dense matter. Science **298**, 1592 (2002). https://doi.org/10.1126/science.1078070
4. H.T. Janka, Explosion mechanisms of core-collapse supernovae. Annu. Rev. Nucl. Part Sci. **62**, 407 (2012). https://doi.org/10.1146/annurev-nucl-102711-094901
5. T.Z. Yan, S. Li, Y.N. Wang et al., Yield ratios and directed flows of light particles from proton-rich nuclei-induced collisions. Nucl. Sci. Tech. **30**, 15 (2019). https://doi.org/10.1007/s41365-018-0534-6
6. Byungsik Hong, Jung Keun Ahn, Gyeonghwan Bak et al., Development of large acceptance multi-purpose spectrometer in Korea for symmetry energy. Nucl. Sci. Tech. **29**, 171 (2018). https://doi.org/10.1007/s41365-018-0507-9
7. B.-J. Cai, L.-W. Chen, Constraints on the skewness coefficient of symmetric nuclear matter within the nonlinear relativistic mean field model. Nucl. Sci. Tech. **28**, 185 (2017). https://doi.org/10.1007/s41365-017-0329-1
8. C. Fuchs, H.H. Wolter, Modelization of the EOS. Eur. Phys. J. A **30**, 5 (2006). https://doi.org/10.1140/epja/i2005-10313-x
9. B.A. Li, L.W. Chen, C.M. Ko, Recent progress and new challenges in isospin physics with heavy-ion reactions. Phys. Rep. **464**, 113 (2008). https://doi.org/10.1016/j.physrep.2008.04.005
10. V. Baran, M. Colonna, V. Greco et al., Reaction dynamics with exotic nuclei. Phys. Rep. **410**, 335 (2005). https://doi.org/10.1016/j.physrep.2004.12.004
11. L.L. Li, Z.H. Li, E.G. Zhao et al., Isospin splitting of the nucleon–nucleus optical potential. Phys. Rev. C **80**, 064607 (2009). https://doi.org/10.1103/PhysRevC.80.064607
12. Q.B. Shen, Y.L. Han, H.R. Guo, Isospin dependent nucleon–nucleus optical potential with Skyrme interactions. Phys. Rev. C **80**, 024604 (2009). https://doi.org/10.1103/PhysRevC.80.024604
13. J.P. Jeuhenne, A. Lejeune, C. Mahaux, Many-body theory of nuclear matter. Phys. Rep. **25**, 85 (1976). https://doi.org/10.1016/0370-1573(76)90017-X
14. L.G. Arnold, B.C. Clark, E.D. Cooper et al., Energy dependence of the p - 40Ca optical potential: a Dirac equation perspective. Phys. Rev. C **25**, 936 (1982). https://doi.org/10.1103/PhysRevC.25.936
15. S. Hama, B.C. Clark, E.D. Cooper et al., Global Dirac optical potentials for elastic proton scattering from heavy nuclei. Phys. Rev. C **41**, 2737 (1990). https://doi.org/10.1103/PhysRevC.41.2737
16. C. Hartnack, J. Aichelin, New parametrization of the optical potential. Phys. Rev. C **49**, 2801 (1994). https://doi.org/10.1103/PhysRevC.49.2801
17. G.Q. Zhang, Y.G. Ma, X.G. Cao et al., Unified description of nuclear stopping in central heavy-ion collisions from 10 MeV to 1.2 GeV. Phys. Rev. C **84**, 034612 (2011). https://doi.org/10.1103/PhysRevC.84.034612
18. J. Aichelin, A. Rosenhauer, G. Peilert et al., Importance of momentum-dependent interactions for the extraction of the nuclear equation of state from high-energy heavy-ion collisions. Phys. Rev. Lett. **58**, 1926 (1987). https://doi.org/10.1103/PhysRevLett.58.1926
19. E.N.E. van Dalen, C. Fuchs, A. Faessler, Effective nucleon masses in symmetric and asymmetric nuclear matter. Phys. Rev. Lett. **95**, 022302 (2005). https://doi.org/10.1103/PhysRevLett.95.022302
20. M. Jaminon, C. Mahaux, Effective masses in relativistic approaches to the nucleon–nucleus mean field. Phys. Rev. C **40**, 354 (1989). https://doi.org/10.1103/PhysRevC.40.354
21. H.Y. Kong, J. Xu, L.W. Chen et al., Constraining simultaneously nuclear symmetry energy and neutron–proton effective mass splitting with nucleus giant resonances using a dynamical approach. Phys. Rev. C **95**, 034324 (2017). https://doi.org/10.1103/PhysRevC.95.034324
22. B.A. Li, X. Han, What can we learn about the neutron–proton effective mass splitting from constraints on the density dependence of nuclear symmetry energy around normal density. Phys. Lett. B **727**, 276 (2013). https://doi.org/10.1016/j.physletb.2013.10.006
23. C.B. Das, S.D. Gupta, C. Gale et al., Momentum dependence of symmetry potential in asymmetric nuclear matter for transport model calculations. Phys. Rev. C **67**, 034611 (2003). https://doi.org/10.1103/PhysRevC.67.034611
24. ChC Moustakidis, Temperature and momentum dependence of single-particle properties in hot asymmetric nuclear matter. Phys. Rev. C **78**, 054323 (2008). https://doi.org/10.1103/PhysRevC.78.054323
25. J.W. Negele, K. Yazaki, Mean free path in a nucleus. Phys. Rev. Lett. **62**, 71 (1981). https://doi.org/10.1103/PhysRevLett.47.71

26. B.A. Li, Constraining the neutron–proton effective mass splitting in neutron-rich matter. Phys. Rev. C **69**, 064602 (2004). https://doi.org/10.1103/PhysRevC.69.064602

27. X.H. Li, W.J. Guo, B.A. Li et al., Neutron–proton effective mass splitting in neutron-rich matter at normal density from analyzing nucleon Cnucleus scattering data within an isospin dependent optical model. Phys. Lett. B **743**, 408 (2015). https://doi.org/10.1016/j.physletb.2015.03.005

28. Z.Q. Feng, Effective mass splitting of neutron and proton and isospin emission in heavy-ion collisions. Nucl. Phys. A **878**, 3 (2012). https://doi.org/10.1016/j.nuclphysa.2012.01.014

29. C. Xu, B.A. Li, L.W. Chen, Symmetry energy, its density slope, and neutron–proton effective mass splitting at normal density extracted from global nucleon optical potentials. Phys. Rev. C **82**, 054607 (2010). https://doi.org/10.1103/PhysRevC.82.054607

30. Z.Q. Feng, Momentum dependence of the symmetry potential and its influence on nuclear reactions. Phys. Rev. C **84**, 024610 (2011). https://doi.org/10.1103/PhysRevC.84.024610

31. E.N.E. van Dalen, C. Fuchs, A. Faessler, Momentum, density, and isospin dependence of symmetric and asymmetric nuclear matter properties. Phys. Rev. C **72**, 065803 (2005). https://doi.org/10.1103/PhysRevC.72.065803

32. W. Zuo, L.G. Cao, B.A. Li et al., Isospin splitting of the nucleon mean field. Phys. Rev. C **60**, 024605 (2005). https://doi.org/10.1103/PhysRevC.72.014005

33. L. Ou, Z. Li, Y. Zhang et al., Effect of the splitting of the neutron and proton effective masses on the nuclear symmetry energy at finite temperatures. Phys. Lett. B **697**, 246 (2011). https://doi.org/10.1016/j.physletb.2011.01.062

34. J. Rizzo, M. Colonna, M. Di Toro et al., Transport properties of isospin effective mass splitting. Nucl. Phys. A **732**, 202 (2004). https://doi.org/10.1016/j.nuclphysa.2003.11.057

35. Z.Q. Feng, Transverse emission of isospin ratios as a probe of high-density symmetry energy in isotopic nuclear reactions. Phys. Lett. B **707**, 83 (2012). https://doi.org/10.1016/j.physletb.2011.12.001

36. W.J. Xie, F.S. Zhang, Nuclear collective flows as a probe to the neutron–proton effective mass splitting. Phys. Lett. B **735**, 250 (2014). https://doi.org/10.1016/j.physletb.2014.06.050

37. Y.X. Zhang, M.B. Tsang, Z. Li et al., Constraints on nucleon effective mass splitting with heavy ion collisions. Phys. Lett. B **732**, 186 (2014). https://doi.org/10.1016/j.physletb.2014.03.030

38. L.W. Chen, C.M. Ko, B.A. Li, Determination of the stiffness of the nuclear symmetry energy from isospin diffusion. Phys. Rev. Lett. **94**, 032701 (2005). https://doi.org/10.1103/PhysRevLett.94.032701

39. H.Y. Kong, Y. Xia, J. Xu et al., Reexamination of the neutron-to-proton-ratio puzzle in intermediate-energy heavy-ion collisions. Phys. Rev. C **91**, 047601 (2015). https://doi.org/10.1103/PhysRevC.91.047601

40. W. Reisdorf, A. Andronic, R. Averbeck et al., (FOPI Collaboration), Systematics of central heavy ion collisions in the 1A GeV regime. Nucl. Phys. A **848**, 366 (2010). https://doi.org/10.1016/j.nuclphysa.2010.09.008

41. A. Andronic, J. Łukasik, W. Reisdorf et al., Systematics of stopping and flow in Au+ Au collisions. Eur. Phys. J. A **30**, 31 (2006). https://doi.org/10.1140/epja/i2006-10101-2

42. F. Rami, Y. Leifels, B. De Schauenburg et al., (FOPI Collaboration), Isospin tracing: a probe of nonequilibrium in central heavy-ion collisions. Phys. Rev. Lett. **84**, 1120 (2000). https://doi.org/10.1103/PhysRevLett.84.1120

43. D. Persram, C. Gale, Elliptic flow in intermediate energy heavy ion collisions and in-medium effects. Phys. Rev. C **65**, 064611 (2002). https://doi.org/10.1103/PhysRevC.65.064611

44. V.R. Pandharipande, S.C. Pieper, Nuclear transparency to intermediate-energy nucleons from (e, e'p) reactions. Phys. Rev. C **45**, 791 (1991). https://doi.org/10.1103/PhysRevC.45.791

45. B.A. Li, L.W. Chen, Nucleon–nucleon cross sections in neutron-rich matter and isospin transport in heavy-ion reactions at intermediate energies. Phys. Rev. C **72**, 064611 (2005). https://doi.org/10.1103/PhysRevC.72.064611

46. Z.Q. Feng, Nuclear in-medium effects and collective flows in heavy-ion collisions at intermediate energies. Phys. Rev. C **85**, 014604 (2012). https://doi.org/10.1103/PhysRevC.85.014604

47. Z.Q. Feng, Nuclear dynamics and particle production near threshold energies in heavy-ion collisions. Nucl. Sci. Tech. **29**, 40 (2018). https://doi.org/10.1007/s41365-018-0379-z

48. P.-C. Li, Y.-J. Wang, Q.-F. Li et al., Collective flow and nuclear stopping in heavy ion collisions in Fermi energy domain. Nucl. Sci. Tech. **29**, 177 (2018). https://doi.org/10.1007/s41365-018-0510-1

49. J. Su, C.Y. Huang, W.J. Xie et al., Effects of in-medium nucleon–nucleon cross sections on stopping observable and ratio of free protons in heavy-ion collisions at 400 MeV/nucleon. Eur. Phys. J. A **52**, 207 (2016). https://doi.org/10.1140/epja/i2016-16207-x

50. F. Zhang, J. Su, A dynamical description of the 136Xe+ p spallation at 1000 MeV/nucleon. Chin. Phys. C **43**, 024103 (2019). https://doi.org/10.1088/1674-1137/43/2/024103

51. J. Aichelin, Quantum molecular dynamics a dynamical microscopic n-body approach to investigate fragment formation and the nuclear equation of state in heavy ion collisions. Phys. Rep. **202**, 233 (1991). https://doi.org/10.1016/0370-1573(91)90094-3

52. G.D. Westfall, W. Bauer, D. Craig et al., Mass dependence of the disappearance of flow in nuclear collisions. Phys. Rev. Lett. **71**, 1986 (1993). https://doi.org/10.1103/PhysRevLett.71.1986